

# Decomposing the role of dry intrusions for ocean evaporation during mistral

Yonatan Givon<sup>1</sup> | Douglas Keller Jr<sup>2</sup> | Romain Pennel<sup>2</sup> | Philippe Drobinski<sup>2</sup> | Shira Raveh-Rubin<sup>1</sup>

<sup>1</sup>Department of Earth and Planetary Sciences, Weizmann Institute of Science, Rehovot, Israel

<sup>2</sup>Laboratoire de Météorologie Dynamique-IPSL, École Polytechnique, Institut Polytechnique de Paris, ENS, PSL Research University, Sorbonne Université, CNRS, Palaiseau, France

## Correspondence

Yonatan Givon, Department of Earth and Planetary Sciences, Weizmann Institute of Science, Rehovot, Israel.

Email: [yonatan.givon@weizmann.ac.il](mailto:yonatan.givon@weizmann.ac.il)

## Funding information

Weizmann-CNRS Collaboration Program; European Cooperation in Science and Technology, Grant/Award Number: CA19109

## Abstract

The mistral is a northerly gap-wind regime blowing through the Rhone Valley in Southern France. It is held responsible for the sea-surface cooling necessary to produce deep convection in the Gulf of Lion through turbulent ocean heat loss. The mistral is tightly connected to lee-cyclogenesis in the Gulf of Genoa, where topography forces substantial downward motion. Dry intrusions (DIs) are airstreams forming the descending branch of extratropical cyclones. Known to induce cold and dry surface anomalies, DIs are potential contributors to enhanced surface evaporation during mistral. In this study, a climatological database (ERA-INTERIM, 1981–2016) of mistral–DI co-occurrence is constructed, allowing quantification of the impact of DIs on the mistral evaporative hot spot for the first time. We find that, on average, mistral–DI evaporation rates are doubled, compared to mistral without DIs. Moreover, cluster-composite analysis reveals amplifications exceeding 300% between dynamically similar mistral events, with response to DIs. Daily latent heat-flux anomalies in the Gulf of Lion are decomposed into contributions from the various parameters to analyse the mistral evaporation response to DIs. Mistral–DI events are shown to produce extreme evaporation rates through increased mistral wind speeds. The results highlight the downward momentum flux delivered by DIs to the mistral at the Gulf of Lion as the primary driver of the evaporation amplification mechanism. We further explore the variability between different mistral–DI events and conclude that extreme mistral–DI evaporation events are linked to descending air trajectories entering the Gulf of Lion at an early stage of their lifetimes. These DIs charge the mistral with maximum vertical momentum fluxes, which act to intensify surface winds and hence evaporation rates.

## KEY WORDS

air-sea interaction, cyclones, Lagrangian airstreams, mediterranean

## 1 | INTRODUCTION

The mistral, renowned as one of the most dangerous wind regimes in the Mediterranean, refers to northerly cold-air outbreaks in the Gulf of Lion (GOL). The mistral is channelled through the Rhone Valley, which separates the Alps from the Massif Central in southern France by a 50-km-wide canyon. Upon the approach of an upper-level trough northwest of the Alps and a corresponding formation of a lee-cyclone in the Gulf of Genoa (GOG), northerly flow is channelled through the Rhone Valley and accelerates across the GOL, generating the mistral wind. Many studies have analysed the mistral from a regional and mesoscale perspective, linking the mistral to mountain-induced gravity-wave activity leading to hydraulic jumps in the boundary layer (Drobinski et al., 2005; Guénard et al., 2006; Jiang et al., 2003). However, the development of northerly flow through the Rhone Valley is attributed to the upper-level trough approaching the Alps (Smith, 1986; Speranza et al., 1985; Tafferner, 1990).

The mistral is known for its contribution to GOG cyclogenesis (Aebischer & Schär, 1998), for example, by generating low-level potential vorticity (PV) banners that wrap around the Genoa cyclone and intensify it. The GOG is one of the most cyclogenetic regions on Earth, with a strong impact on society, economy, and well-being in the region (Flaounas et al., 2022). In a recent review of Alpine cyclogenesis theories, the mistral wind (alongside other gap-wind regimes in the Mediterranean) is pointed out as one of the main remaining challenges for the numerical modelling of the process. This is due to the high impact of small-scale orographic features on the mistral wind speed (WS; Obermann-Hellund & Ahrens, 2018), and its tight connection to the cyclone's deepening rate (Alpert et al., 1996; Mattocks & Bleck, 1986). An improved understanding of the topographic influence on upper-level PV evolution is proposed to improve the understanding of mistral and Alpine lee-cyclogenesis (Buzzi et al., 2020). Such an effort was recently carried out by Givon et al. (2021) and will be discussed further here.

Composed of cold and dry air and accompanied by intense WSs, the mistral generates an evaporation hot spot in the GOL (Lebeaupin Brossier & Drobinski, 2009; Millot, 1979; Schott et al., 1996). The evaporation rates attributed to the mistral are extreme, with surface latent heat fluxes (SLHF) exceeding  $-1000 \text{ W} \cdot \text{m}^{-2}$  during intense mistral events (Bunker, 1972; Flamant, 2003). Such extreme evaporation rates were reported to reduce sea-surface temperatures in the GOL significantly and affect following precipitation events in southern France (Berthou et al., 2014). The moisture picked up by the mistral contributes to maintenance of the Genoa cyclone by

latent heat release (Homar et al., 2003), and the cooling of the sea surface contributes to deep convection in the GOL, an important link in the chain of Mediterranean oceanic circulation (Herrmann et al., 2017; Waldman et al., 2017). Mistral events are often short (1–2 days) but can also last a week or more, making their contribution to the gradual destabilization of the GOL water column more meaningful. Keller et al. (2022) showed the role of the mistral in the build-up process of deep convection for winter 2012–2013 and suggested that long and/or a frequent succession of shorter mistral events is needed during the build-up season (approximately October–January), for the destabilization process of the GOL water column to reach the threshold for the initiation of deep convection. Keller et al. (2023, in review) enhanced said analysis to 20 years and concluded that variations in seasonal stratification play a key role in the evolution of deep convection. However, since a high-pass filter is used to separate the mistral forcing from the seasonal, the long-term part of the mistral appears to handle a considerable part of the variability of the 'seasonal' part. Thus, the mistral contribution to deep convection in the GOL is difficult to isolate.

While these air-sea interactions of the mistral wind are well documented, the contribution from the different parameters of the evaporation bulk equation to the GOL evaporation rates is not generally known (Lebeaupin Brossier et al., 2012; Menezes et al., 2019). Since the mistral is a northerly gap-wind regime, blowing from land towards the sea, it has a strong advective nature in terms of temperature and humidity. Still, the evaporative response to the mistral varies strongly during events, and between them. Thus, another process appears to be modulating the intense evaporation rates in the GOL during mistral events, besides the horizontal advection. A possible source of this variability could be related to the vertical motion of mistral air parcels.

In his study, McGinley (1982) reported the importance of the topographically induced vertical stretching of air parcels in the lee of the Alps as a major source of vorticity in Alpine lee-cyclogenesis. Jiang et al. (2003) specifically addressed the descending nature of the mistral wind, caused by the downward tilting of isentropic surfaces on the lee side of the Alps. The topographic effect of the Alps acts in constructive interaction with upper-level PV advection (Tsidulko & Alpert, 2001), cooling the air column along the lagging cold front and causing subsidence of isentropic surfaces with velocities of ca 5 hPa per hour. While this downward forcing is rather local, in many cases it appears spatially and temporally aligned with the orientation of large-scale dry intrusions. Dry intrusions (DIs) are rapidly descending air streams ( $>400 \text{ hPa}$  in 48 hr), Raveh-Rubin, (2017), forming the descending branch of extratropical cyclones (Browning, 1997;

Thorncroft et al., 1993; Wernli & Davies, 1997). DIIs usually originate below the tropopause, upstream of an upper-level trough, and descend slantwise towards the cold sector of the surface cyclone. These dry and cold airstreams interact with the surface and generate a wide range of weather extremes, ranging from wind and precipitation compound extremes (Raveh-Rubin & Wernli, 2015, 2016) to dust storms (Fluck & Raveh-Rubin, 2023a, 2023b), temperature extremes (Klaider & Raveh Rubin, 2023), and the spread of wildfires (Magaritz-Ronen & Raveh-Rubin, 2023). DIIs were shown to enhance vertical mixing in the boundary layer (Ilotoviz et al., 2021), and enhance ocean evaporation (Rai & Raveh-Rubin, 2023; Raveh-Rubin & Catto, 2019). The response of surface WSs to DIIs is not conclusive; however, several studies suggest the vertical transfer of horizontal momentum by DIIs as a possible driver of extreme cross-frontal wind gusts (Browning & Reynolds, 1994; Raveh-Rubin & Wernli, 2015). Thus, it is reasonable to assume that DIIs will yield a similar amplifying impact on the mistral-generated evaporation hot spot, due to their increased surface winds, dryness, or both. A recent study (Silverman et al., 2021) successfully used a convolutional neural network to predict the location of DI initiation, based solely on geopotential fields at three pressure levels. This view links DI origin to the upper-level forcing, which may be understood in greater detail using isentropic upper-level PV structures. The mistral and Alpine lee-cyclogenesis processes are extremely sensitive to the different upper-level PV distributions driving them (Mattocks & Bleck, 1986; Tafferner, 1990). Givon et al. (2021) performed a climatological classification of upper-level PV distributions during all mistral events in the 1981–2016 period based on ECMWF ERA-Interim data to address this nonlinear mode of variability. Sixteen well-defined clusters appear, with clear seasonal separation and a distinct surface impact, in terms of WSs, temperatures, precipitation, pressure, and turbulent surface latent (and sensible) heat flux. Each cluster corresponds to a different life stage of the mistral-driving Rossby wave, from initiation through the mature, phase-lock stage to Rossby wave-breaking (RWB) and cut-off formations. It is shown that as the PV streamer is advected across the Alps, the evaporative features of the mistral intensify significantly.

Despite the importance of mistral evaporation to the initiation of deep convection in the GOL, and the well-understood downward motion attributed to the mistral, the mechanism linking mistral evaporation rates to the presence of DIIs was never directly evaluated. Here, we use the mistral and DI climatological datasets to assess the contribution of DIIs to mistral evaporation rates.

This study addresses the following questions:

1. What are the dominant controlling factors of evaporation in the GOL under mistral?
2. How do atmospheric conditions and evaporative response change under mistral embedded in DIIs and what is the underlying mechanism?

The methods to detect mistral and DIIs are given in Section 2, along with the surface latent heat-flux decomposition and a simplistic derivation of the vertical momentum flux (VMF). The results are displayed in Section 3, and a summarizing discussion follows in Section 4.

## 2 | DATA AND METHODS

### 2.1 | Atmospheric data

The main data source for this study are ECMWF ERA-INTERIM data (Dee et al., 2011), on a 6-hr temporal resolution, interpolated to 1° spatial resolution. The period of 1 September 1981, to 1 September 2016, is analysed. Anomalies are defined as deviations from gridded monthly climatology.

### 2.2 | Mistral identification

We base the climatological analysis on the daily mistral dataset introduced by Givon et al. (2021). In this climatological mistral dataset, objective mistral identification is based on a surface cyclone detected in the cyclone domain (Figure 1), using ERA-INTERIM reanalysis, and northerly flow exceeding  $2 \text{ m}\cdot\text{s}^{-1}$  in the Rhone Valley using WRF-ORCHIDEE data in higher resolution (see Givon et al., 2021 for more details). This objective definition results in 2734 mistral days throughout the period of 1981–2016, corresponding to 21% annual mean frequency, ranging from 33% in February to 10% in June–July.

### 2.3 | Mistral-DI identification

We distinguish between mistral days in which DIIs are found in the GOL from days when such DIIs are absent, by using a Lagrangian-based identification of DIIs, as follows. Forward air mass trajectories are calculated using LAGRANTO (Sprenger & Wernli, 2015), and DIIs are then identified as trajectories that exceed a descent threshold of 400 hPa within 48 hr, as in Raveh-Rubin (2017). We define the DI target domain as a rectangular cube at 41–44° N, 3–6° E, from the surface and up to 700 hPa in

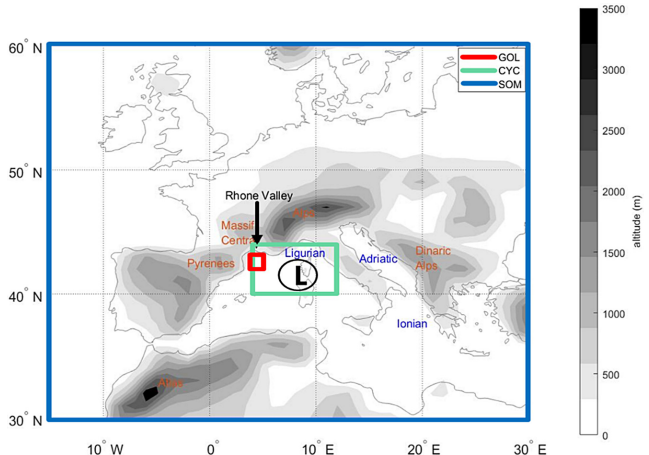


**FIGURE 1** ERA-INTERIM topography (shading) and domains used to define the mistral wind and classify the upper-level forcing. For a day to be accounted for as a mistral, the presence of a surface cyclone is demanded in the cyclone (CYC) domain and northerly flow in the Gulf of Lion (GOL) domain. Daily mean, upper-level, isentropic (320–340 K) potential vorticity (PV) distributions are recorded in the self-organizing map (SOM) domain for the self-organizing map clustering analysis of Givon et al. (2021).

the vertical (red box in Figure 3). Mistral days in which a non-zero number of DI trajectories enter the DI target domain are hereby registered as mistral–DI days, allowing a 1° tolerance level for the actual location of DIs relative to the DI target domain. This Eulerian approach, defining a DI outflow object (e.g., Catto & Raveh-Rubin, 2019), has proven significant in earlier studies to demonstrate a low-level response to the presence of DIs, yet it does not allow for a Lagrangian analysis of the corresponding DI trajectories. Therefore, we complement the Eulerian approach with a fully Lagrangian one. For this, we track individual DI trajectories that travel through the DI target domain. DI trajectories are attributed to mistral if they are present within the DI target domain at a pressure exceeding 700 hPa during a mistral day. If there is no mistral upon the DI's arrival at the DI target domain, the DI is classified as non-mistral and is secluded from the analysis. We focus on the more inclusive Eulerian approach for identifying events and use the full Lagrangian approach to analyse vertical momentum transfer (Subsection 2.2). DI trajectories are attributed to mistral clusters based on their time of arrival at the DI target domain. We further examine the evolution of the DI air masses along their trajectory into the GOL and therefore track the following variables along the DI trajectory: horizontal WS, vertical velocity, and the time of entry into the DI target domain relative to the start of their 48-hr descent.

## 2.4 | SLHF decomposition

In ERA-Interim, the SLHF is parametrized using the bulk formula (Brodeau et al., 2017, ECMWF IFS Documentation Cy31r1):

$$Q_l = L_v C_e \rho_a WS(q_a - q_s), \quad (1)$$

where  $Q_l$  refers to SLHF,  $L_v$  is the latent heat of evaporation ( $2.5 \times 10^6 \text{ J} \cdot \text{kg}^{-1}$ ),  $C_e$  the drag coefficient ( $\sim 0.003$ ),  $\rho_a$  air density (using the ideal gas approximation,  $\rho_a = \frac{p_{\text{surface}}}{RT_{2-\text{m}}}$ ),  $WS$  is  $WS$  taken at the 10-m level, and  $q_s, q_a$  are specific humidity in saturation at sea-surface temperature and in-situ air, respectively, on the 900-hPa level. To evaluate the leading parameters governing ocean evaporation under the mistral, and their response under DI conditions, we adopt the evaporation decomposition method from Menezes et al. (2019). Equation (1) can be rewritten in terms of sea-surface temperature (SST), near-surface stability ( $S = T_{2-\text{m}} - SST$ ), relative humidity (RH) at the 900-hPa level, and  $WS$  to yield:

$$Q_l = L_v C_e \rho_a WS q_0 [\exp(\beta SST) - RH \exp(\beta (SST + S))], \quad (2)$$

The full differential can be developed for anomalies:

$$\begin{aligned} Q'_l = & \frac{\partial Q_l}{\partial SST} SST' + \frac{\partial Q_l}{\partial S} S' + \frac{\partial Q_l}{\partial RH} RH' \\ & + \frac{\partial Q_l}{\partial WS} WS' + \frac{\partial Q_l}{\partial \rho_a} \rho'_a, \end{aligned} \quad (3)$$

where the prime denotes anomalies defined as deviations from the monthly mean ( $x' = x - \bar{x}$ ). Note that in ERA-INTERIM  $C_e$  mainly changes as a function of surface features (vegetation, land humidity, etc.) which are irrelevant for the region of interest in the GOL. Thus, and due to its small contribution as shown by earlier studies (Bosilovich et al., 2017; Richter & Xie, 2008), variance in the drag coefficient is neglected. Each partial derivative has been evaluated numerically to give:

$$\frac{\partial Q_l}{\partial SST} = Q_l \frac{\alpha (\beta / SST^2 - c / SST)}{-RH [\beta / (SST + S)^2 - c / (SST + S)]},$$

$$\frac{\partial Q_l}{\partial S} = Q_l \frac{RH [\beta / (SST + S)^2 - c / (SST + S)]}{[\alpha - RH]},$$

$$\frac{\partial Q_l}{\partial RH} = -\frac{Q_l}{\alpha - RH},$$

$$\frac{\partial Q_l}{\partial WS} = \frac{Q_l}{WS},$$

$$\frac{\partial Q_l}{\partial \rho_a} = \frac{Q_l}{\rho_a},$$

where:

$$\alpha = \exp\left(\frac{\beta}{SST + S} - \frac{\beta}{SST} - c \ln\left(\frac{SST}{SST + S}\right)\right);$$

$$\beta = 6743.769; c = 4.8451.$$

Thus, the SLHF anomaly is decomposed, and the contribution of each parameter is quantified. All terms are averaged across the GOL domain to evaluate the different contributions to mistral evaporation. As noted by Menezes et al. (2019), the contributions of RH, S, and SST cannot be fully decoupled, as they are also found in the numerical approximations of the other terms. However, these are absolute values, not anomalies, and variations of the different contributions are mainly attributed to the corresponding anomalies. Here, the decomposition and the following reconstruction (Equation 3) successfully evaluate the evaporation flux anomaly taken directly from ERA-Interim. The daily correlation between the daily mean reanalysed values and the reconstructed ones for our study period (1981–2016) is 0.92. The average contribution to evaporation from the different terms is evaluated, as is the net difference in latent heat flux between DI and non-DI mistral events.

## 2.5 | Vertical momentum flux

The notion of vertical transfer of horizontal momentum from upper to lower levels under DI conditions as a source of increased frontal gusts was suggested by Browning and Reynolds (1994). However, VMFs are usually considered on turbulent scales. Here, we quantify the vertical transport of horizontal momentum on synoptic timescales, by evaluating the DI horizontal and vertical velocities. While the horizontal WS is known along the trajectory by construction in the Lagrangian approach using reanalysis data, the vertical velocity is translated from pressure to height coordinates, via the height-log-pressure relationship. Specifically, for a reference height scale  $H$  and reference surface pressure  $p_0$ , the log-pressure coordinate can be written as follows (Hoffmann, 2012; Holton & Hakim, 2012):

$$Z \log P = -H \cdot \log\left(\frac{p}{p_0}\right),$$

Thus, the vertical velocity  $W$  of the DI at each time step can be approximated using:

$$W = \frac{\Delta(Z \log P)}{\Delta t},$$

Choosing  $H = 7500$  m, and taking the product of the vertical velocity  $W$  and horizontal WS at the DI air-mass position provides an estimation of the vertical flux of horizontal momentum (hereafter, VMF) applied by the DI towards the surface:

$$VMF \equiv W \cdot |V|,$$

where  $|V|$  here is the horizontal WS at the location of the DI. Since the focus here is on the downward flux of large WSs, only the size of the horizontal wind is considered; thus, negative VMF indicates downward momentum transport, while positive VMF stands for upward momentum transport. The VMF usually peaks in the early stage of DIs, when both horizontal and vertical WSs are largest, as most DIs consist of an upper-level perturbation and a gradual decay of vertical (and horizontal) WS towards the surface (Raveh-Rubin, 2017).

## 3 | RESULTS

### 3.1 | Statistical link between DI and mistral

Throughout 1981–2016, we find that 23% of all mistral days (2734 days) are accompanied by a non-zero DI outflow in the DI target domain, corresponding to 636 mistral-DI days. In the analysis that follows, mistral-DI days are considered strictly for mistral days, without any extension to the mistral duration, based on the Eulerian DI outflow identification. Regarding the Lagrangian DI trajectories, 7068 DIs travel through the DI target domain during 738 days. A slight majority (4235 trajectories forming 55% of DI days, i.e., 406 days) of these DI days occur together with a mistral, accounting for 15% of mistral days. Most of the non-mistral DI trajectories arrive at the DI target domain adjacently to mistral events; for example, if mistral days are expanded to include a two-day lag, ca 80% of all DIs entering the GOL are captured within the mistral period. Thus, DIs in the GOL are indeed tightly linked to the mistral. Figure 2 outlines the surface impact of mistral and mistral-DI events in the GOL. In the absence of mistral, WSs are mostly below  $10 \text{ m} \cdot \text{s}^{-1}$ , the RH is greater than 60%, and SLHF rarely exceeds  $-200 \text{ W} \cdot \text{m}^{-2}$ . Under mistral only, WSs increase up to  $15 \text{ m} \cdot \text{s}^{-1}$ , while RH decreases down to 50%, leading to SLHF of down to  $-400 \text{ W} \cdot \text{m}^{-2}$ .

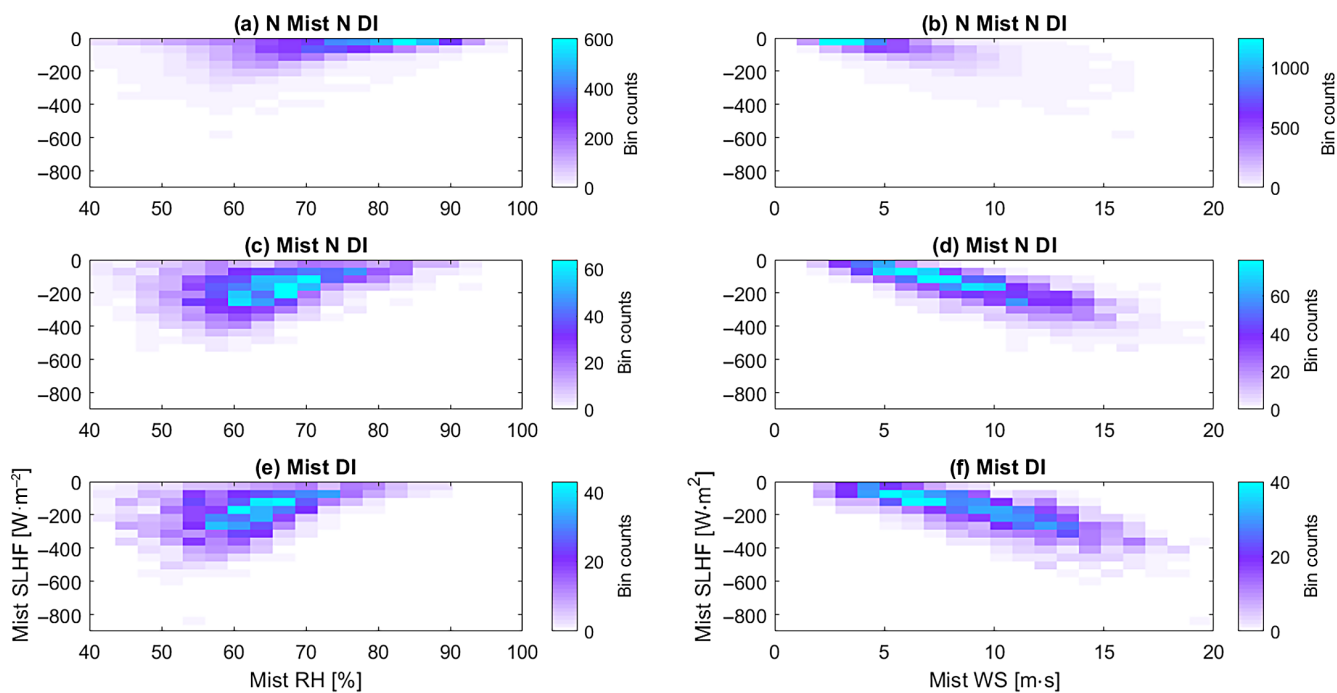


**FIGURE 2** Probability-density plots of Gulf of Lion (GOL) 900 hPa RH and surface latent heat flux (SLHF, left column) and GOL 10-m WS and SLHF (right column), differentiating between no-mistral days (top), mistral-no DI (middle), and mistral-DI (bottom), for 1 September 1981–1 September 2016, based on daily averaged ERA-INTERIM data in the GOL box (Figure 1).

**TABLE 1** Association between surface daily mean extremes in the Gulf of Lion (GOL) and mistral/mistral-dry intrusions (DI) days.

Parameter	Threshold	Fraction of extremes occurring during mistral	Fraction of mistral extremes accompanied by a mistral-DI
10-m WS	>15 (99th percentile)	89%	48%
900-hPa RH	<55% (98th percentile)	33%	37%
SLHF	<-300 W · m⁻² (95th percentile)	83%	41%
SSHF	<-85 W · m⁻² (95th percentile)	84%	36%
dSST/dt	<-0.5 K · day⁻¹ (90th percentile)	49%	40%

Abbreviations: RH, relative humidity; SLHF, surface latent heat fluxes; SSHF, surface sensible heat flux; SST, sea-surface temperature; WS, wind speed.

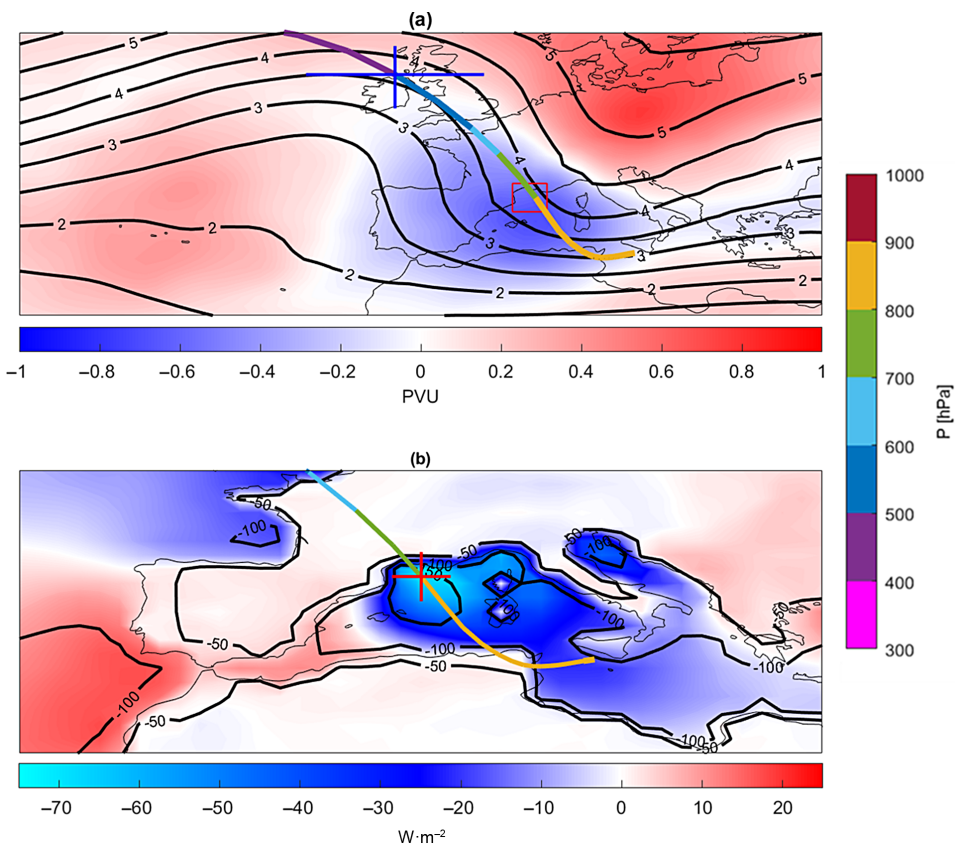
In the presence of DI, however, WS intensifies further and approaches  $20 \text{ m} \cdot \text{s}^{-1}$  more often, while RH drops to as low as 40%, leading to extreme evaporation SLHF exceeding  $-500 \text{ W} \cdot \text{m}^{-2}$ .

From an extreme-event perspective, Table 1 summarizes the probabilities of several meteorological extremes in the GOL to be associated with mistral/DI days. While mistral-DIs compose a mere 23% of all mistral days, they form 48% (37%) of the extreme 10-m WS (RH) threshold. That is, mistral-DI days compose almost one half of the extreme WS and RH mistral days, suggesting a considerable part of the climatological mistral signature can be attributed to the added impact of DIs. Similarly, ca 40% of extreme mistral SLHF, surface sensible heat flux, and

sea-surface cooling occurs under mistral-DI days. In terms of conditional probability, the DI-related extreme frequencies (Table 1, right column) approach almost twice that of the climatological DI frequency out of all mistral events (23%). This suggests a dramatic impact of DI on extreme weather events occurring during mistral, particularly for extreme 10-m winds.

On average, Figure 3 suggests that latent heat flux at the GOL increases by ca 50% in response to DIs, compared to total mistral mean. This anomaly has a large spatial extent, covering the northwestern and central Mediterranean, as well as the Adriatic Sea (Figure 3b). Under DI conditions, not only the near-surface atmospheric parameters change, but the

**FIGURE 3** Mean mistral (black contours) and net differences (shading) in (a) upper-level isentropic potential vorticity (PV) (PVU, 320–340 K mean) and (b) surface latent heat fluxes ( $\text{W} \cdot \text{m}^{-2}$ ) between mistral events with DIs minus mistral events without DIs. The DI target domain is shown by the red box. The coloured line denotes the mean position and pressure height (colour, hPa) of the 4235 mistral-DI trajectories. The blue and red crosses denote the two standard deviations of the trajectory's locations 6 and 36 hr, respectively, after their start of 400-hPa descent.



large-scale, upper-tropospheric setting of the mistral differs from the mean mistral conditions. Mistral-DIs correspond to a deeper trough above Europe and a more tilted Atlantic ridge indicative of RWB and enhancing the PV gradient across Central Europe. The mean arrival time of DIs to the DI target domain stands on 36 hr after initiation of their descent, with ca 70% of these trajectories beginning their descent over the Atlantic, initially forced by a remote Atlantic trough (not shown). Roughly 30% of these DI trajectories, however, start in Central Europe, in response to the local PV anomaly driving the mistral. These appear to undergo an even steeper descent as they travel a relatively shorter horizontal distance to the GOL. In Subsection 3.4 and Figure A1, we further evaluate the diverse forms of DI impact by examining it on the different mistral clusters.

### 3.2 | SLHF decomposition

Dry intrusions are known to be drier due to their upper-level origins compared to the ambient air mass at the GOL (Figure 1) and entail higher near-surface WSs (Figure 2, Table 1) and lower static stability (Ilo-toviz et al., 2021; Raveh-Rubin, 2017). As all these components potentially promote enhanced SLHF, to better understand how DIs are mechanistically associated with

an increase in the mistral SLHF signature, decomposition and reconstruction of SLHF anomalies in the GOL are performed. Using this tool, the response of SLHF to DI occurrence during mistral events is quantified with attribution to the leading factors. We reconstruct the reanalysed SLHF time series at the GOL, using Equation (3); Figure 4a shows an example section of the time series for the extended winter of 2012–2013, showing the dominance of mistral and DI events on GOL evaporation rates. The SLHF anomaly is shown in blue by subtracting the long-term monthly climatology of SLHF from the daily field. The main discrepancies between the reanalysed and reconstructed time series are the underestimation of positive values (mild surface condensation) and the overestimation of negative extremes (evaporation). The largest reconstructed overestimation is shown in Figure 4: on 28 October, an intense Mistral-DI event generated SLHF anomalies of  $-800 [\text{W} \cdot \text{m}^{-2}]$ , while  $-1500 [\text{W} \cdot \text{m}^{-2}]$  is reported by the reconstruction. While these negative biases only appear above a certain threshold of the SLHF anomaly and possibly indicate nonlinear synergy between the evaporation drivers, addressing this nonlinearity is beyond our current scope. Nevertheless, the correlation between the anomaly and the reconstruction is  $\sim 0.92$  throughout the period, in agreement with Menezes et al. (2019), allowing further analysis of the evaporation drivers.

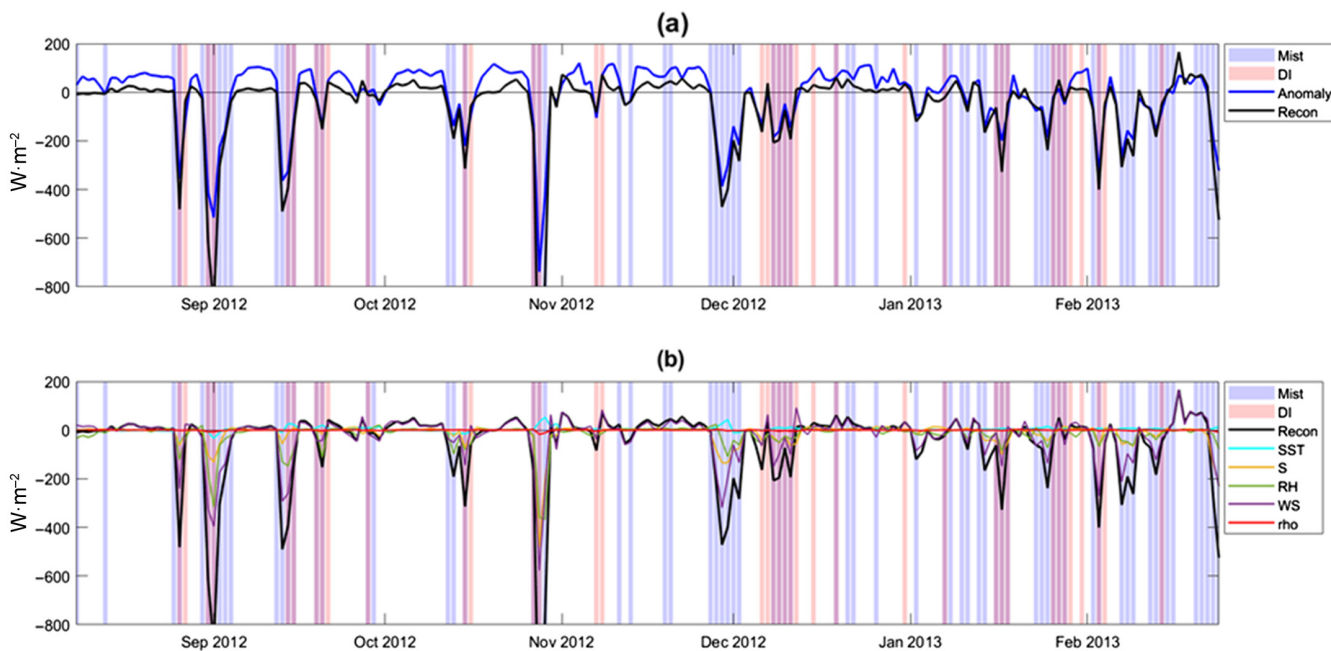


**FIGURE 4** (a) An illustrative time series of surface latent heat flux (SLHF) anomaly (Anomaly) and reconstruction (Recon) in  $\text{W} \cdot \text{m}^{-2}$ , shown for the extended winter season of 2012–2013 out of the full analysis period. The correlation coefficient between the anomaly and reconstruction for the entire dataset is 0.92. (b) As in (a) but with SLHF reconstruction and decomposition to the five terms on the right-hand side of Equation (3): sea-surface temperature (SST), surface stability ( $S$ ), relative humidity (RH), wind speed (WS), air density ( $\rho$ ). All parameters are daily averaged within the GOL domain (Figure 1). Mistral and DI days are denoted by the blue and red bars, respectively, and their overlap is denoted by purple bars.

The decomposition suggests surface WSs (purple line in Figure 4b) as the primary driver of SLHF variability in the mistral case (with  $\sim 50\%$  mean contribution of the WS term, Figure 5), with surface stability ( $S$ ) and RH providing a comparable, smaller contribution. The contribution from anomalies in SST and air density is an order of magnitude smaller, with SST often having an opposite (positive) contribution. This can be understood as negative feedback by SST anomalies on evaporation rates, that is, evaporation cools the sea surface, which creates a negative SST anomaly that reduces evaporation. The advective nature of the mistral is clear in the temporal evolution of the event: WS anomalies appear first, driving RH and instability ( $S$ ) due to the northerly (cold) descending (dry) orientation of the mistral.

The SLHF decomposition (Figure 5) confirms the dominance of mistral WS as the primary driver of evaporation in the GOL, with an average factor of 2 over the secondary contributions of RH and  $S$ . Quantifying the contribution to SLHF from the different terms with and without DIs suggests that the increased mistral SLHF under DI conditions also stems from increased WS. While the general decrease of RH and  $S$ , and the increase of WS under DIs all favour enhanced SLHF, their relative contributions vary. Although the relative response of RH to the presence of DI is larger than that of WS, the net

contribution of the latter is greater. The decrease in RH and  $S$  under DI conditions each leads to changes on the order of  $-50 \text{ W} \cdot \text{m}^{-2}$ , while increased WSs generate differences exceeding  $-100 \text{ W} \cdot \text{m}^{-2}$ . In relative terms, the contributions from the various anomalies are similar with or without DI. In the no-DI mistral events, WS forms 54% of mistral evaporation, while RH and  $S$  contribute 24% and 21%, respectively. Under the influence of DIs, WS handles 51%, while RH and  $S$  contribute 30% and 18%, respectively. While the difference in median evaporation rates between mistral with and without DIs is on a scale of  $100 \text{ W} \cdot \text{m}^{-2}$ , the edges of the two distributions suggest much larger case-to-case variability. This motivates a closer look into the mistral response to DI under the different mistral classes (Givon et al., 2021), to possibly identify flow types that are more sensitive to the presence of DI than others.

### 3.3 | Cluster analysis

To account for the large variability among mistral events, we inspect the distribution of DIs across the different mistral clusters presented in Givon et al. (2021). With this approach, we analyse the modified dynamical environment in the presence of DIs in terms of the large- and synoptic-scale setting. We examine the spatial variability of

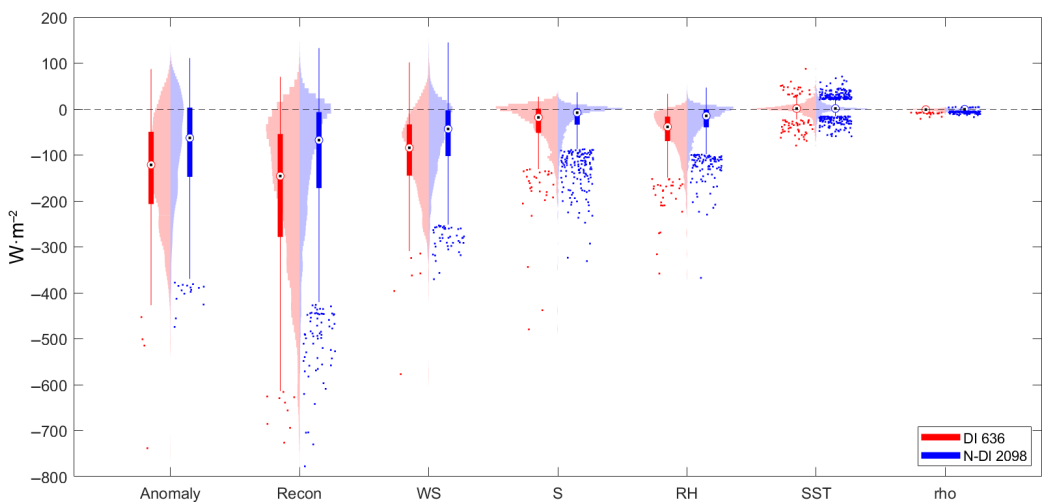


**FIGURE 5** Boxplots and corresponding histograms of surface latent heat flux (SLHF) anomaly (Anomaly), SLHF reconstruction (Recon), and contributions from anomalies of wind speed (WS), surface stability (S), relative humidity (RH), sea-surface temperature (SST), and air density ( $\rho$ ), during mistral-DI events (red) and mistral events without DIs (blue). The black dots show median values, and the boxes extend between the top and bottom quartiles. Whiskers mark the 2.5 and 97.5 percentiles of the distribution and define the limits for the outliers. The numbers in the legend give the number of DI and mistral days in the dataset. The histograms are normalized by bin counts.

the evaporation response to DIs among clusters (Figure 6). Mistral-DI frequency varies sharply between the clusters, with 36% frequency corresponding to 50 mistral-DI days in cluster 7 and down to 9% corresponding to 13 mistral-DI days for the summer cut-off cluster 1 when indeed DIs are climatologically less frequent (Raveh-Rubin, 2017).

Figure 6 breaks down the DI impact on the SLHF decomposition to the different mistral flow types (clusters). For a given cluster, variations between events with and without DIs show significant differences in SLHF, with median amplification approaching 150 W·m<sup>-2</sup>, exceeding 300% amplification compared to mistral no-DI in some clusters (1, 5, 6, and 8). Weaker amplification is shown in other clusters (9, 11, and 13), and only cluster 7 shows a reduction of evaporation rates in response to DI. Examining the different terms composing the SLHF anomaly, it is clear across most clusters that variations in WS form the bulk of DI amplification (~50%), though RH anomalies also contribute considerably (~30%). The stability term  $S$  supplies the third-largest contribution (~20%). Variations in SST and air density are an order of magnitude smaller and are therefore not displayed. With that said, the secondary components RH and  $S$  do seldom appear as leading contributors to evaporation. The secondary contribution of  $S$  and RH changes the amplified SLHF signal under DIs differently in the different seasons. The summer clusters (2, 5) exhibit some of the largest amplified SLHF signals, which the secondary terms further enhance. Differently, the amplified signal of the winter clusters 15 and 16 is significantly contributed to by the secondary terms, while differences in the leading

WS term are smaller. To gain insight into the sources of the cluster differences, we now examine the large- and synoptic-scale systems that differ by cluster.

From the PV perspective, Figure 3 suggests that mistral-DI is related to later stages of the Rossby-wave evolution compared to mistral without DIs. Figure 7 further illustrates with different Rossby-wave lifecycles, that most PV features display a southeastward shift of the PV trough in association with DI. Anticyclonic RWB patterns are generally re-enforced (namely clusters 1, 5, 8, 9, and 13), that is, the meridional PV gradient reversal is amplified under the influence of DIs. Following the mean DI pressure levels, it appears that DIs originating closer to the GOL tend to descend more steeply. This feature is best illustrated by the DI composite of cluster 1. Such steep DIs are rare, and hence their presence is obscured in larger composites (Figure 3a). More details about the DI origins are given in Appendix A.

The DI link to the Genoa cyclone (Figure 8) reveals that the surface cyclone is usually deeper when DIs occur, as is the Atlantic ridge, implying increased sea level pressure gradients across the orography. Cluster 7 interestingly shows a weakening of the Genoa cyclone, corresponding to a weakening of the upper-level PV signature above and the SLHF hot spot. Noting that this cluster displays a phase-lock structure, it appears that the easterly shift in upper-level PV is tilting the wave out of phase, resulting in an easterly tilt that weakens the surface cyclone upon the arrival of DIs.

As shown in Figure 9, the mistral-DI SLHF signature is amplified throughout most of the clusters by over 100%. The DI impact is evident well beyond the GOL,

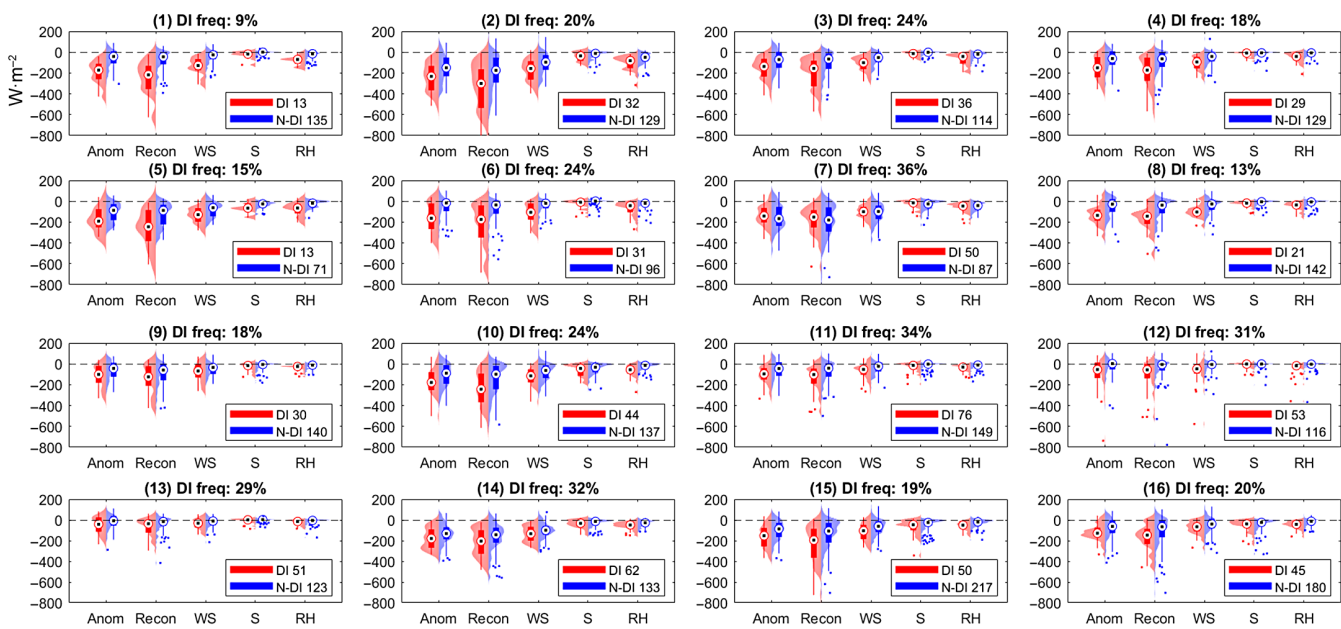


FIGURE 6 As Figure 5, differentiating among 16 mistral clusters.

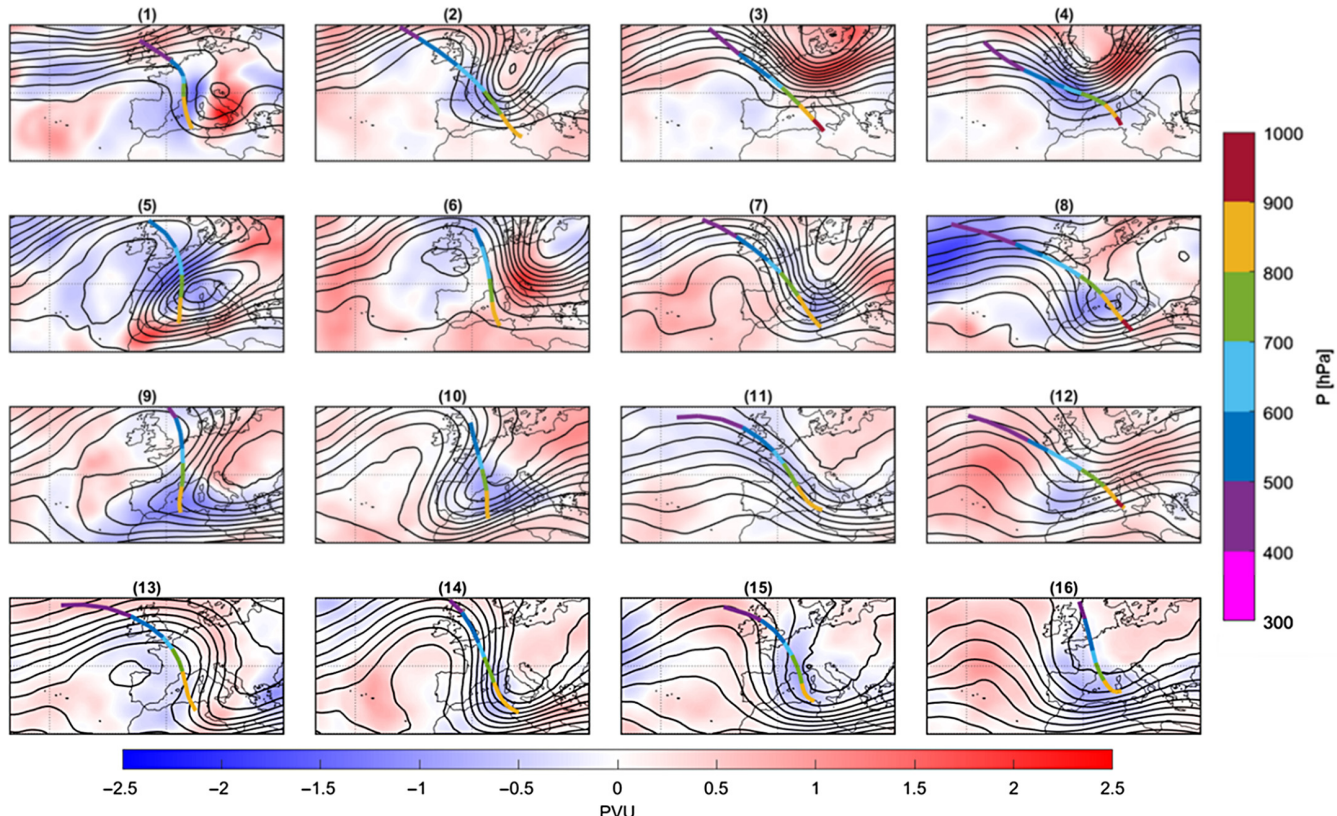
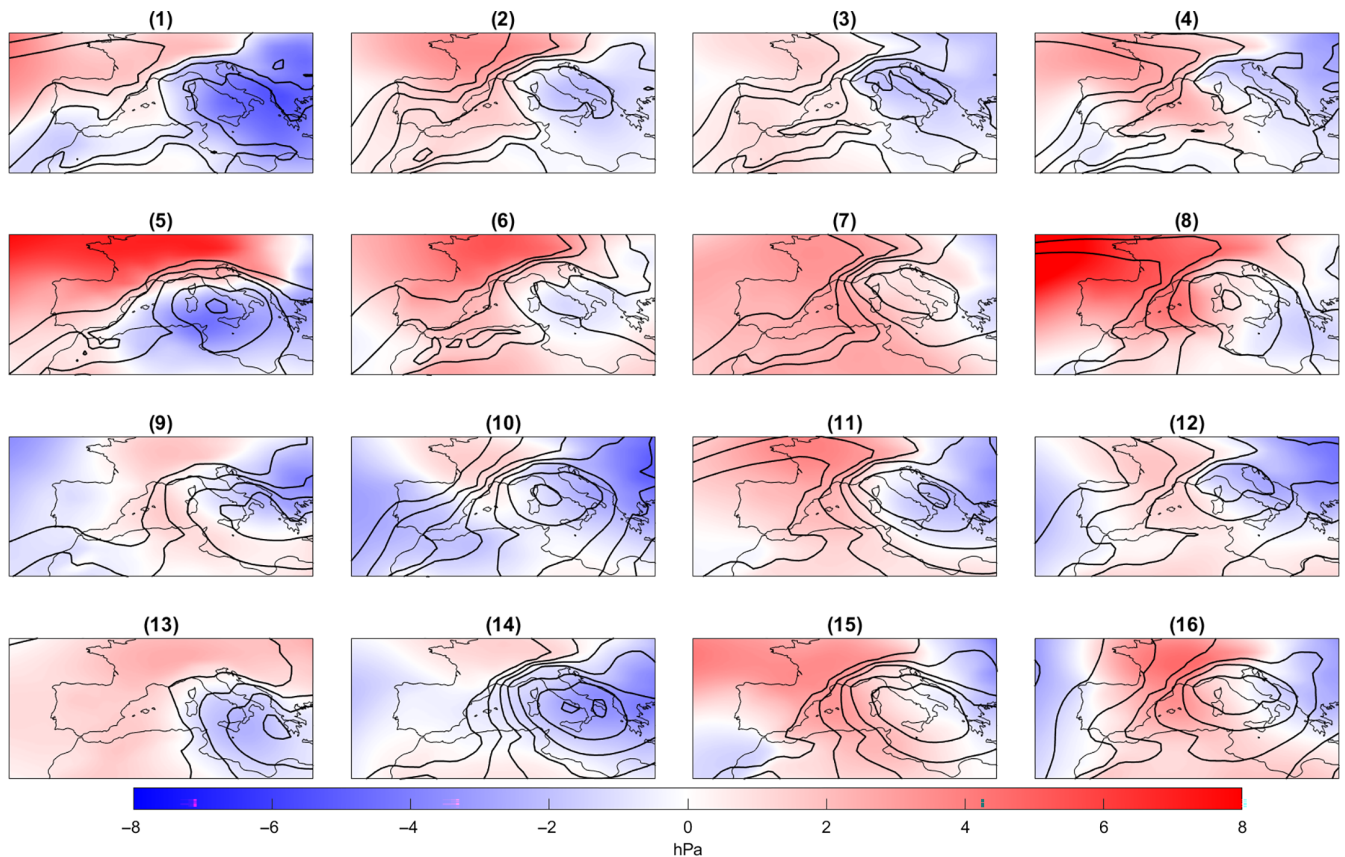


FIGURE 7 Composites of isentropic potential vorticity (PV), averaged within 320–340 K (black contour, 0.5 PVU intervals) of the mistral classes derived in Givon et al. (2021), overlaid with composite PV anomaly (difference between mistral events with dry intrusion (DI) and without DI, shading, in PVU). The coloured line in each cluster stands for the mean position and pressure height (colour, hPa) of the DI trajectories in this cluster. More details on the spatial distribution of the DI trajectories are provided in Appendix A.



**FIGURE 8** As Figure 7, but for the composite difference in sea level pressure (SLP) between mistral events with and without dry intrusions (DIs), on a smaller domain.

varying in extent and amplitude between the mistral clusters. Also, positive SLHF anomalies over land act to increase the land-sea temperature contrast, with further implications for the cyclone's deepening and mistral WSs. As the mistral clusters are seasonally separate, Figure 9 also shows that the DI impact on the mistral is especially strong during the summer (clusters 1–4) and transition seasons (clusters 5–8) compared to winter (clusters 9–16), despite being less frequent then. Still, major differences are present even between clusters that share a seasonal distribution (e.g., 2–3, 7–8).

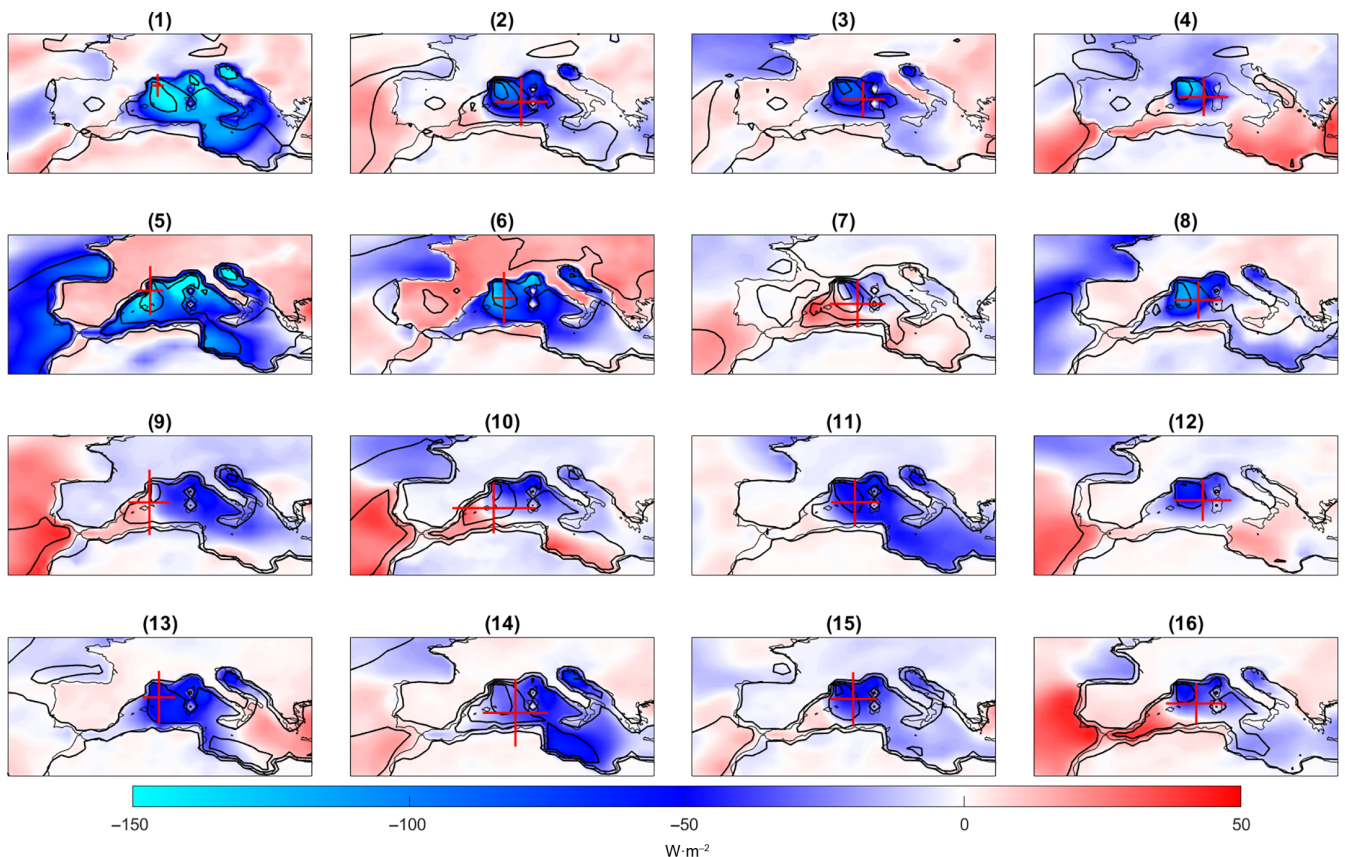
### 3.4 | Mistral-DI amplification mechanism

While the link between DIs and low RH is self-explanatory, the increase in mistral WS in the presence of DIs is not trivial. It has been suggested that vertical transport of horizontal momentum (or VMF) is acting to deliver some of the large momentum DIs possess at the upper levels towards the surface (Browning & Golding, 1995). However, this relationship has never been quantified from the Lagrangian perspective of DI trajectories or

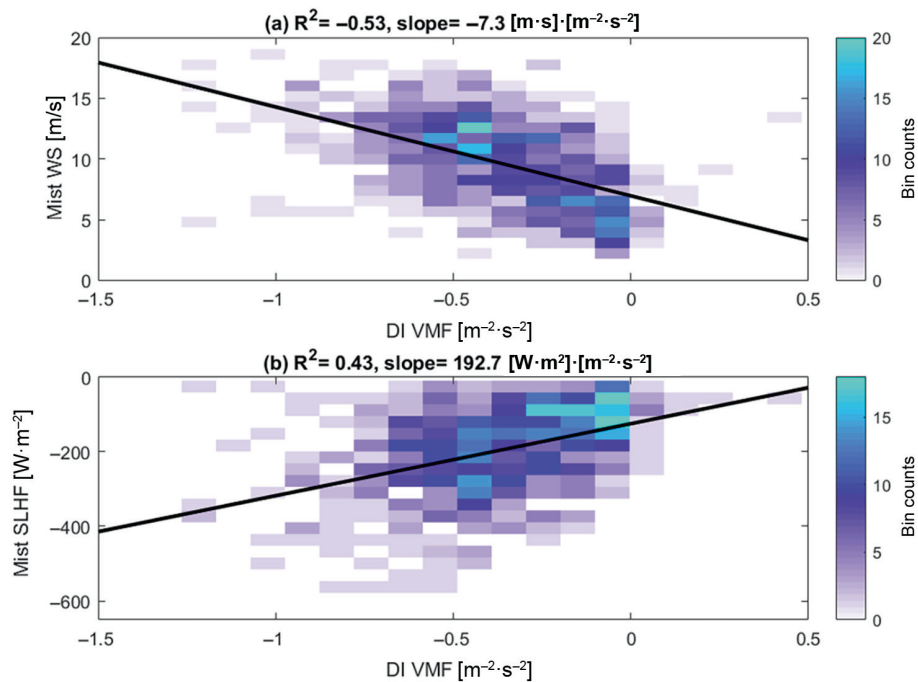
generalized on a climatological time scale. Here, the DI VMF is calculated along each trajectory (corresponding to  $\sim 80 \text{ km} \times 80 \text{ km} \times 20 \text{ hPa}$  air parcel volumes), and its relationship with the mistral surface winds and heat fluxes in the GOL is explored using linear correlation and regression coefficients.

Figure 10 shows the link between VMF and SLHF, through increased surface winds. The downward momentum flux (negative DI VMF) is correlated to mistral WS at 10 m in the GOL (Figure 10a). Thus, DI VMF is also well correlated with enhanced evaporation in the GOL (negative SLHF, Figure 10b). Yet, there is large variation among mistral-DI days.

Based on the linear regression coefficients (in Figure 10b), an extreme negative DI VMF anomaly of  $1 \text{ m}^2 \cdot \text{s}^{-2}$  is anti-correlated to a positive anomaly of ca  $7 \text{ m} \cdot \text{s}^{-1}$  in mistral WS, equivalent to an amplification of ca  $-190 \text{ W} \cdot \text{m}^{-2}$  in SLHF. These numbers agree well with the average range of intensification of negative  $100\text{--}200 \text{ W} \cdot \text{m}^{-2}$  in mistral SLHF under DI conditions, stemming mostly from wind-related anomalies. Notably, SLHF approaching  $-500 \text{ W} \cdot \text{m}^{-2}$  appears exclusively with VMF larger in magnitude than  $0.5 \text{ m}^2 \cdot \text{s}^{-2}$ . These statistical results suggest VMF as a key factor



**FIGURE 9** As Figure 8, but for the net difference in surface latent heat fluxes (SLHFs) between mistral events with and without dry intrusions (DIs) (shaded). Red cross indicates the spatial variability of the DI outflow as in Figure 3b.



**FIGURE 10** Probability-density plot of (a) daily mean DI vertical flux of horizontal momentum (VMF) (x-axis) with mistral 10-m wind speed, and (b) mistral surface latent heat fluxes (SLHFs). Mistral variables are averaged within the Gulf of Lion. The linear best fit is denoted by the black line. Correlation coefficients ( $R^2$ ) are displayed in the title as well as the linear best fit ('slope') in units of [predictor]/[precursor].

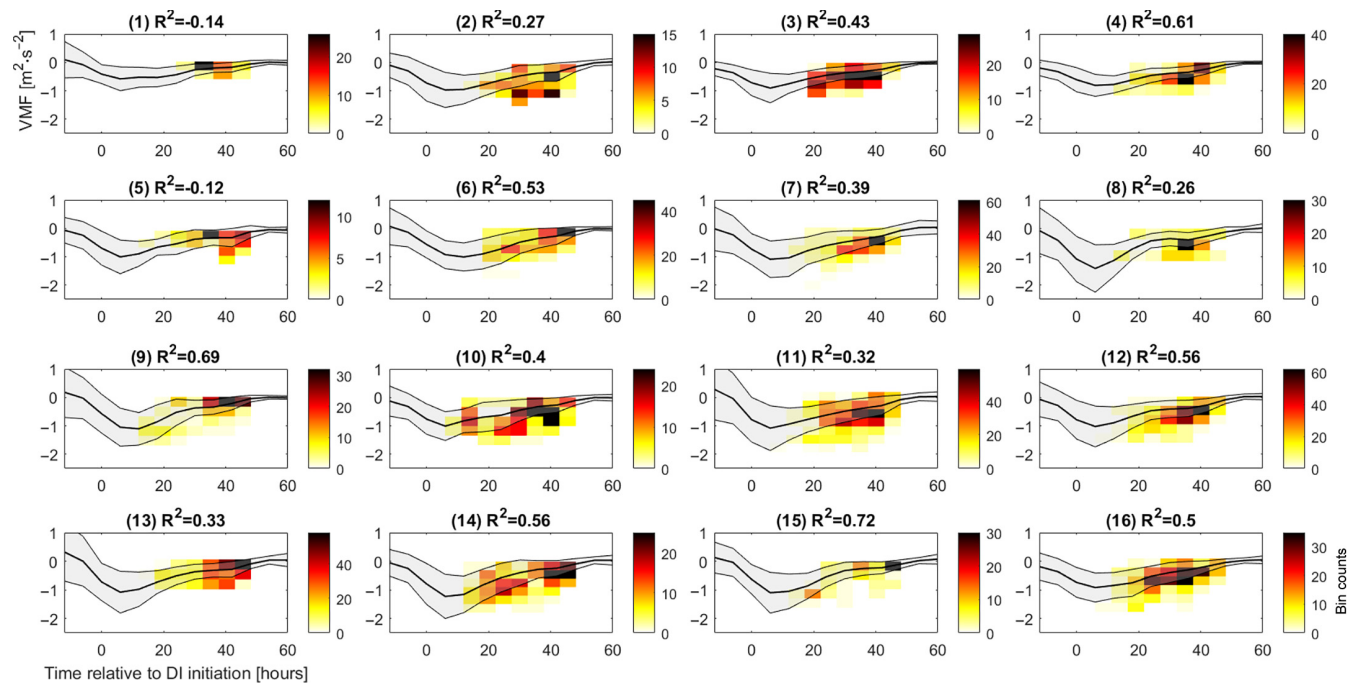


**FIGURE 11** Cluster mean vertical momentum flux (VMF) time evolution along the dry intrusions (DI) ( $\pm 1$  standard deviation, line and shading). The DI descends 400 hPa in the time window 0–48 hr by construction. Overlaid is a density plot of the vertical flux of horizontal momentum (VMF) in the Gulf of Lion and the time of DI entry to the DI target domain. Correlation coefficients between VMF at the GOL and relative DI time of entry at the DI target domain are given in the title of each panel.

controlling mistral–DI interactions. To assess variations in VMF delivered to the mistral in the GOL region, a linear correlation regression analysis is performed. The results show that the VMF delivered to the mistral is linked to the time in which the trajectory enters the DI target domain relative to the start of its slantwise descent. The relative time of entry is correlated ( $R^2 \sim 0.48$ , not shown) to the distance between the DI at time 0 and its destination in the GOL. Recalling the DI target domain is limited in the vertical to 700 hPa, suggesting that early entering DIs correspond to rapidly descending trajectories, originating closer to the GOL. These air masses travel the vertical path from the upper to the lower troposphere faster and thus reach lower levels with substantially larger VMF. Therefore, we expect DIs originating near the GOL to embed the mistral at a relatively early stage of their descent and to deliver maximum VMF towards the surface. To understand the variations in VMF, we correlate the relative arrival time of a given DI at the target domain, to the VMF it delivers at the corresponding time step.

Figure 11 shows the distribution of VMF throughout the DI trajectory, separated by clusters. Typically, VMF maximizes at the first stages of DIs (Figure 11), when vertical and horizontal velocities usually peak in the upper troposphere. The VMF peak amplitude and width change among clusters and within them, with notably cluster 8 exceeding negative  $2 \text{ m}^2 \cdot \text{s}^{-2}$ . The decay of VMF towards

the surface also varies among the clusters, with some appearing to consist of a first peak that decays with time, while other clusters consist of a slower, or at times halted, decay of VMF closer to the GOL. Figure 11 also includes the Eulerian link between the approaching DI and VMF at the GOL. For most of the clusters, the linear correlation between DI arrival time and VMF at the corresponding DI time step is stronger than the total mean taking all clusters together ( $\sim 0.47$ ). In the clusters with relatively slower Lagrangian decay of VMF (e.g., 1, 2, 5) the correlation between the DI arrival time to the GOL and the VMF is lower as the trend of the mean VMF is virtually flat. Yet the response to DI outflow can be dramatic, apparently due to the still large VMF (i.e., cluster 2). These results support a relationship in which DIs that originate closer to the GOL experience a steeper descent and deliver maximum VMF anomalies. Specifically, a negative VMF anomaly of  $1 \text{ m}^2 \cdot \text{s}^{-2}$  is equivalent to a DI entering the GOL 12 hr earlier than average ( $\sim 36$  hr). This relationship between the DI time, VMF, and SLHF in the GOL suggests a mechanism linking all aspects of the mistral evaporation response to DI.

Figure 12 illustrates schematically the mechanism mediating DI VMF and mistral SLHF (see Appendix B, Figure B1). DIs starting closer to the GOL (DI2) enter the domain earlier. These trajectories lose less momentum along the path compared to more distant DIs (i.e., DI1). This may be explained by the horizontal WS decay towards

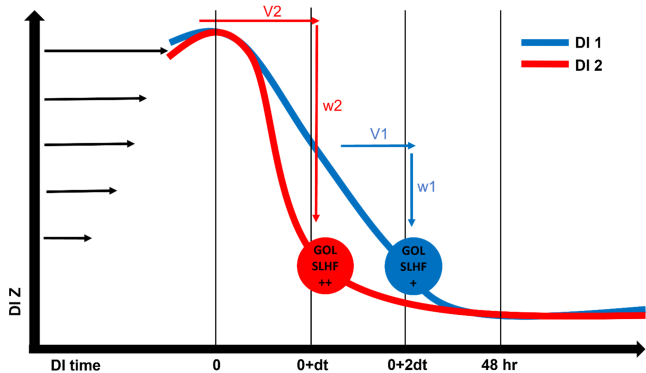


**FIGURE 12** Schematic summarizing the relationship between the arrival time of a given dry intrusion (DI) to the Gulf of Lion (GOL), and the corresponding surface latent heat fluxes (SLHF), mediated by vertical momentum flux. Each coloured line stands for a different form of DI, with DI2 (red) denoting steeper DIs, and DI1 (blue) denoting moderately descending trajectories. Horizontal ( $V_1, V_2$ ) and vertical ( $w_1 w_2$ ) wind vectors corresponding to each illustrative DI track are denoted with horizontal and vertical arrows, respectively. The arrival of both trajectories to the GOL on different time steps is marked by coloured circles, whose shades illustrate the relative intensity of SLHF in the GOL, with the red colour corresponding to more intense evaporation rates. The ambient vertical zonal-wind shear is represented by the black arrows and forms the source of horizontal momentum for the DI.

the surface, and/or by weaker vertical motions. The two act to reduce the VMF delivered to the mistral by (relatively) slowly descending DIs.

#### 4 | SUMMARY AND DISCUSSION

This study analyses the response of the mistral wind to the presence of DI outflow and particularly its impact on ocean evaporation in the GOL. We find that almost 90% of extreme WSs in the GOL occur during mistral days, and the same holds for extreme evaporation events (see Table 1), half of which are attributed to the added impact of DIs. Furthermore, we note that the co-occurrence of mistral and DIs constitute the driest and most intense mistral events, where evaporation rates tend to maximize. The mistral plays a key role in the build-up process of deep convection in the GOL by triggering strong evaporation, and DIs are shown to mostly enhance the mistral-induced evaporation. We first characterize mistral events in the presence of DIs and find a median amplification of  $\sim 100 \text{ W} \cdot \text{m}^{-2}$  in evaporation under DI influence, corresponding to a ca 50% increase compared to an average mistral event, and a ca 100% increase compared to an average no-DI mistral event. Menezes et al. (2019) decomposed SLHF during dry air outbreaks in the Red Sea, with

results suggesting RH as the primary driver of evaporation. We similarly decompose daily SLHF anomalies in the GOL into their controlling terms, showing, differently, that mistral evaporation in general and specifically the increased SLHF in mistral-DI events is primarily due to increased WSs. We further inspect how this response varies between the mistral clusters (Givon et al., 2021). Mistral-DI mostly occurs with a deeper surface cyclone and upper-level trough, corresponding to stronger winds and enhanced evaporation. Correlation and linear regression analysis further pinpoint the importance of VMF as a pathway through which DIs increase low-level WSs, hence increasing SLHF.

Addressing the two questions raised in the introduction, we here conclude that the dominant term controlling the mistral SLHF signal is the near-surface WS, with WS anomalies responsible for ca 50% of the SLHF anomaly, and the rest divided rather equally between RH and surface stability ( $S$ ) anomalies. Despite several studies addressing the role of increased SST for ocean evaporation in future climate projections (Adloff et al., 2015; Drobinski et al., 2018; Somot et al., 2008; Somot et al., 2018), we find both the SST and air-density anomalies make up only a non-significant fraction of the mistral evaporation anomaly, at this time scale. In their October 2012 mistral case study, Rainaud et al. (2017) separated the SLHF in the GOL into dynamic and thermodynamic terms — the first primarily corresponds to surface winds while the latter merges the surface stability ( $S$ ) and RH effects — to conclude that the thermodynamics are dominating the SLHF. Indeed, if the  $S$  and RH terms here were combined in an equivalent way, their contribution appears to match or slightly surpass that of WS. However, in the more detailed decomposition presented here, WS appears as the primary driver for mistral evaporation. DIs increase the mistral evaporation signal partly by low moisture content and decreased surface stability, but more so due to increased WSs which are shown to be stemming from VMFs. The DI impact on the mistral varies significantly between different mistral flow structures, with most clusters being strongly affected while the most intense (e.g., cluster 7) and weakest mistral (e.g., cluster 13) phases are only weakly affected.

Correlation and linear regression suggest that, on average, DIs entering the DI target domain relatively early in their lifetimes (i.e., 10 hr earlier than the average time of  $\sim 35$  hr) show maximum VMF anomalies of the order of  $-1 \text{ m}^2 \cdot \text{s}^{-2}$ . These VMF anomalies correspond to mean anomalies of  $-190 \text{ W} \cdot \text{m}^{-2}$  in SLHF, delivered primarily by increased WSs. These numbers agree well with the observed amplification of SLHF during mistral-DI events by over  $-200 \text{ W} \cdot \text{m}^{-2}$ , leading to the conclusion that VMF is indeed crucial for mediating the mistral response to DIs.

These results highlight the importance of DIs to the mistral evaporative features and highlight the role of the mistral as an upper-level-to-surface pathway in which upper-tropospheric momentum is transported downwards into the GOL in the form of DIs, bearing profound influence on mistral air-sea interactions, and further contributing to deep water formation (Keller et al., 2022, 2023). These results stress the importance of improving our understanding and predictive ability of downward motions in the atmosphere, and their future projections and implications.

## AUTHOR CONTRIBUTIONS

Yonatan Givon performed the analysis, produced the figures, and drafted the manuscript. Shira Raveh-Rubin supervised the research, and together with Philippe Drobinski acquired research funding. All co-authors reviewed and edited the manuscript.

## ACKNOWLEDGEMENTS

This article is based upon work from COST Action CA19109 ‘European network for Mediterranean cyclones in weather and climate’ supported by COST (European Cooperation in Science and Technology, <https://www.medcyclones.eu/>). The Israel Meteorological Service and ECMWF are acknowledged for providing access to ERA-Interim data. This work was supported by the Weizmann–CNRS Collaboration Program and by the Maggie Kaplan Research Fund, the de Botton Center for Marine Science, and the Sustainability and Energy Research Initiative at the Weizmann Institute of Science.

## CONFLICT OF INTEREST STATEMENT

The authors have no competing interests to declare.

## DATA AVAILABILITY STATEMENT

Data available on request from the authors.

## ORCID

*Yonatan Givon*  <https://orcid.org/0000-0003-1171-2823>

*Shira Raveh-Rubin*  <https://orcid.org/0000-0001-6244-8693>

## REFERENCES

- Adloff, F., Somot, S., Sevault, F., Jordà, G., Aznar, R., Déqué, M. et al. (2015) Mediterranean Sea response to climate change in an ensemble of twenty first century scenarios. *Climate Dynamics*, 45, 2775–2802. Available from: <https://doi.org/10.1007/s00382-015-2507-3>
- Aebischer, U. & Schär, C. (1998) Low-level potential vorticity and cyclogenesis to the lee of the Alps. *Journal of the Atmospheric Sciences*, 55(2), 186–207. Available from: [https://doi.org/10.1175/1520-0469\(1998\)055<0186:LLPVAC>2.0.CO;2](https://doi.org/10.1175/1520-0469(1998)055<0186:LLPVAC>2.0.CO;2)
- Alpert, P., Tsidulko, M., Krichak, S. & Stein, U. (1996) A multi-stage evolution of an ALPEX cyclone. *Tellus A*, 48(2), 209–220. Available from: <https://doi.org/10.1034/j.1600-0870.1996.t01-1-00002.x>
- Berthon, S., Mailler, S., Drobinski, P., Arsouze, T., Bastin, S., Béranger, K. et al. (2014) Prior history of mistral and tramontane winds modulates heavy precipitation events in southern France. *Tellus A*, 66(1), 24064 <https://hal.archives-ouvertes.fr/hal-01130284>.
- Bosilovich, M.G., Robertson, F.R., Takacs, L., Molod, A. & Mocko, D. (2017) Atmospheric water balance and variability in the MERRA-2 reanalysis. *Journal of Climate*, 30(4), 1177–1196. Available from: <https://doi.org/10.1175/JCLI-D-16-0338.1>
- Brodeau, L., Barnier, B., Gulev, S.K. & Woods, C. (2017) Climatologically significant effects of some approximations in the bulk parameterizations of turbulent air-sea fluxes. *Journal of Physical Oceanography*, 47(1), 5–28. Available from: <https://doi.org/10.1175/JPO-D-16-0169.1>
- Browning, K.A. (1997) The dry intrusion perspective of extra-tropical cyclone development. *Meteorological Applications*, 4(4), 317–324. Available from: <https://doi.org/10.1017/S1350482797000613>
- Browning, K.A. & Golding, B.W. (1995) Mesoscale aspects of a dry intrusion within a vigorous cyclone. *Quarterly Journal of the Royal Meteorological Society*, 121(523), 463–493. Available from: <https://doi.org/10.1002/qj.49712152302>
- Browning, K.A. & Reynolds, R. (1994) Diagnostic study of a narrow cold-frontal rainband and severe winds associated with a stratospheric intrusion. *Quarterly Journal of the Royal Meteorological Society*, 120(516), 235–257. Available from: <https://doi.org/10.1002/qj.49712051602>
- Bunker, A.F. (1972) Wintertime interactions of the atmosphere with the Mediterranean Sea. *Journal of Physical Oceanography*, 2(3), 225–238. Available from: [https://doi.org/10.1175/1520-0485\(1972\)002<0225:WIOTAW>2.0.CO;2](https://doi.org/10.1175/1520-0485(1972)002<0225:WIOTAW>2.0.CO;2)
- Buzzi, A., Davolio, S. & Fantini, M. (2020) Cyclogenesis in the lee of the Alps: a review of theories. *Bulletin of Atmospheric Science and Technology*, 1, 433–457. Available from: <https://doi.org/10.1007/s42865-020-00021-6>
- Catto, J.L. & Raveh-Rubin, S. (2019) Climatology and dynamics of the link between dry intrusions and cold fronts during winter. Part I: global climatology. *Climate Dynamics*, 53, 1873–1892. Available from: <https://doi.org/10.1007/s00382-019-04745-w>
- Dee, D.P., Uppala, S.M., Simmons, A.J., Berrisford, P., Poli, P., Kobayashi, S., Andrae, U., Balmaseda, M.A., Balsamo, G., Bauer, P., Bechtold, P., Beljaars, A.C.M., van de Berg, L., Bidlot, J., Bormann, N., Delsol, C., Dragnani, R., Fuentes, M., Geer, A.J., ... Vitart, F. (2011) The ERA-Interim reanalysis: configuration and performance of the data assimilation system. *Quarterly Journal of the Royal Meteorological Society*, 137(656), 553–597. Portico. <https://doi.org/10.1002/qj.828>
- Drobinski, P., Bastin, S., Guénard, V., Caccia, J.L., Dabas, A.M., Delville, P. et al. (2005) Summer mistral at the exit of the Rhône valley. *Quarterly Journal of the Royal Meteorological Society*, 131(605), 353–375. Available from: <https://doi.org/10.1256/qj.04.63>
- Drobinski, P., Da Silva, N., Panthou, G., Bastin, S., Muller, C., Ahrens, B. et al. (2018) Scaling precipitation extremes with temperature in the Mediterranean: past climate assessment and projection in anthropogenic scenarios. *Climate Dynamics*, 51, 1237–1257. Available from: <https://doi.org/10.1007/s00382-016-3083-x>

- Flamant, C. (2003) Alpine lee cyclogenesis influence on air-sea heat exchanges and marine atmospheric boundary layer thermodynamics over the western Mediterranean during a tramontane/mistral event. *Journal of Geophysical Research: Oceans*, 108(C2). Available from: <https://doi.org/10.1029/2001JC001040>
- Flaounas, E., Davolio, S., Raveh-Rubin, S., Pantillon, F., Miglietta, M.M., Gaertner, M.A. et al. (2022) Mediterranean cyclones: current knowledge and open questions on dynamics, prediction, climatology and impacts. *Weather and Climate Dynamics*, 3(1), 173–208. Available from: <https://doi.org/10.5194/wcd-3-173-2022>
- Fluck, E. & Raveh-Rubin, S. (2023a) Dry air intrusions link Rossby wave breaking to large-scale dust storms in Northwest Africa: four extreme cases. *Atmospheric Research*, 286, 106663. Available from: <https://doi.org/10.1016/j.atmosres.2023.106663>
- Fluck, E. & Raveh-Rubin, S. (2023b) A 16-year climatology of the link between dry air intrusions and large-scale dust storms in North Africa. *Atmospheric Research*, 106844, 106844. Available from: <https://doi.org/10.1016/j.atmosres.2023.106844>
- Givon, Y., Keller, D., Jr., Silverman, V., Pennel, R., Drobinski, P. & Raveh-Rubin, S. (2021) Large-scale drivers of the Mistral wind: link to Rossby wave life cycles and seasonal variability. *Weather and Climate Dynamics*, 2(3), 609–630. Available from: <https://doi.org/10.5194/wcd-2-609-2021>
- Guénard, V., Drobinski, P., Caccia, J.L., Tedeschi, G. & Currier, P. (2006) Dynamics of the MAP IOP 15 severe mistral event: observations and high-resolution numerical simulations. *Quarterly Journal of the Royal Meteorological Society*, 132(616), 757–777. Available from: <https://doi.org/10.1256/qj.05.59>
- Herrmann, M., Auger, P.A., Ulses, C. & Estournel, C. (2017) Long-term monitoring of ocean deep convection using multisensors altimetry and ocean color satellite data. *Journal of Geophysical Research: Oceans*, 122(2), 1457–1475. Available from: <https://doi.org/10.1002/2016JC011833>.
- Hoffmann, C.G. (2012) Application of CO as a tracer for dynamics in the polar winter middle atmosphere: A study based on ground-based microwave observations in Kiruna (Doctoral dissertation, Universität Bremen). Available at: <http://nbn-resolving.de/urn:nbn:de:gbv:46-00102610-19>.
- Holton, J. R., and Hakim, G. J. (2012). *An introduction to dynamic meteorology*. Waltham, MA: Academic Press (Elsevier), 245 (Vol. 88).
- Homar, V., Romero, R., Stensrud, D.J., Ramis, C. & Alonso, S. (2003) Numerical diagnosis of a small, quasi-tropical cyclone over the western Mediterranean: dynamical vs. boundary factors. *Quarterly Journal of the Royal Meteorological Society*, 129(590), 1469–1490. Available from: <https://doi.org/10.1256/qj.01.91>
- Ilotoviz, E., Ghate, V.P. & Raveh-Rubin, S. (2021) The impact of slantwise descending dry intrusions on the marine boundary layer and air-sea interface over the ARM eastern North Atlantic site. *Journal of Geophysical Research: Atmospheres*, 126(4), e2020JD033879. Available from: <https://doi.org/10.1029/2020JD033879>
- Jiang, Q., Smith, R.B. & Doyle, J. (2003) The nature of the mistral: observations and modelling of two MAP events. *Quarterly Journal of the Royal Meteorological Society*, 129(588), 857–875. Available from: <https://doi.org/10.1256/qj.02.21>
- Keller, D., Jr., Givon, Y., Pennel, R., Raveh-Rubin, S. & Drobinski, P. (2022) Untangling the mistral and seasonal atmospheric forcing driving deep convection in the Gulf of Lion: 2012–2013. *Ocean Science*, 18, 483–510. Available from: <https://doi.org/10.5194/os-18-483-2022>
- Keller, D., Jr., Givon, Y., Pennel, R., Raveh-Rubin, S. & Drobinski, P. (2023) Untangling the mistral and seasonal atmospheric forcing driving deep convection in the Gulf of lion: 1993–2013. *Journal of Geophysical Research Oceans* (under review). Available from: <https://doi.org/10.1002/essoar.10512293.1>
- Klaider, N., & Raveh-Rubin, S. (2023). Extended influence of mid-latitude cyclones on global cold extremes. *Geophysical Research Letters*, 50(20), e2023GL104999.
- Lebeaupin Brossier, C. & Drobinski, P. (2009) Numerical high-resolution air-sea coupling over the Gulf of lions during two tramontane/mistral events. *Journal of Geophysical Research: Atmospheres*, 114(D10). Available from: <https://doi.org/10.1029/2008JD011601>
- Lebeaupin Brossier, C., Drobinski, P., Béranger, K., Bastin, S. & Orain, F. (2012) Ocean memory effect on the dynamics of coastal heavy precipitation preceded by a mistral event in the northwestern Mediterranean. *Quarterly Journal of the Royal Meteorological Society*, 139(675), 1583–1597. Available from: <https://doi.org/10.1002/qj.2049>
- Magaritz-Ronen, L. & Raveh-Rubin, S. (2023) Tracing the formation of exceptional fronts driving historical fires in Southeast Australia. *npj Climate and Atmospheric Science*, 6(1), 110–119. Available from: <https://doi.org/10.1038/s41612-023-00425-z>
- Mattocks, C. & Bleck, R. (1986) Jet streak dynamics and geostrophic adjustment processes during the initial stages of lee cyclogenesis. *Monthly Weather Review*, 114(11), 2033–2056. Available from: [https://doi.org/10.1175/1520-0493\(1986\)114<2033:JSDAGA>2.0.CO;2](https://doi.org/10.1175/1520-0493(1986)114<2033:JSDAGA>2.0.CO;2)
- McGinley, J. (1982) A diagnosis of alpine lee cyclogenesis. *Monthly Weather Review*, 110(9), 1271–1287. Available from: [https://doi.org/10.1175/1520-0493\(1982\)110<1271:ADOALC>2.0.CO;2](https://doi.org/10.1175/1520-0493(1982)110<1271:ADOALC>2.0.CO;2)
- Menezes, V.V., Farrar, J.T. & Bower, A.S. (2019) Evaporative implications of dry-air outbreaks over the northern Red Sea. *Journal of Geophysical Research: Atmospheres*, 124(9), 4829–4861. Available from: <https://doi.org/10.1029/2018JD028853>
- Millot, C. (1979) Wind induced upwellings in the Gulf of lions. *Oceanologica Acta*, 2(3), 261–274.
- Obermann-Hellund, A. & Ahrens, B. (2018) Mistral and tramontane simulations with changing resolution of orography. *Atmospheric Science Letters*, 19(9), e848. Available from: <https://doi.org/10.1002/asl.848>
- Rai, D. & Raveh-Rubin, S. (2023) Enhancement of Indian summer monsoon rainfall by cross-equatorial dry intrusions. *npj Climate and Atmospheric Science*, 6, 43. Available from: <https://doi.org/10.1038/s41612-023-00374-7>
- Rainaud, R., Brossier, C.L., Ducrocq, V. & Giordani, H. (2017) High-resolution air-sea coupling impact on two heavy precipitation events in the Western Mediterranean. *Quarterly Journal of the Royal Meteorological Society*, 143(707), 2448–2462. Available from: <https://doi.org/10.1002/qj.3098>
- Raveh-Rubin, S. (2017) Dry intrusions: Lagrangian climatology and dynamical impact on the planetary boundary layer. *Journal of Climate*, 30(17), 6661–6682. Available from: <https://doi.org/10.1175/JCLI-D-16-0782.1>
- Raveh-Rubin, S. & Catto, J.L. (2019) Climatology and dynamics of the link between dry intrusions and cold fronts during winter, part II: front-centred perspective. *Climate Dynamics*, 53(3–4),

- 1893–1909. Available from: <https://doi.org/10.1007/s00382-019-04793-2>
- Raveh-Rubin, S. & Wernli, H. (2015) Large-scale wind and precipitation extremes in the Mediterranean: a climatological analysis for 1979–2012. *Quarterly Journal of the Royal Meteorological Society*, 141(691), 2404–2417. Available from: <https://doi.org/10.1002/qj.2531>
- Raveh-Rubin, S., & Wernli, H. (2016). Large-scale wind and precipitation extremes in the Mediterranean: dynamical aspects of five selected cyclone events. *Quarterly Journal of the Royal Meteorological Society*, 142(701), 3097–3114. Portico. <https://doi.org/10.1002/qj.2891>
- Richter, I. & Xie, S.P. (2008) Muted precipitation increase in global warming simulations: a surface evaporation perspective. *Journal of Geophysical Research: Atmospheres*, 113(D24). Available from: <https://doi.org/10.1029/2008JD010561>
- Schott, F., Visbeck, M., Send, U., Fischer, J., Stramma, L. & Desaubies, Y. (1996) Observations of deep convection in the Gulf of lions, northern Mediterranean, during the winter of 1991/92. *Journal of Physical Oceanography*, 26(4), 505–524. Available from: [https://doi.org/10.1175/1520-0485\(1996\)026<0505:OOCIT>2.0.CO;2](https://doi.org/10.1175/1520-0485(1996)026<0505:OOCIT>2.0.CO;2)
- Silverman, V., Nahum, S. & Raveh-Rubin, S. (2021) Predicting origins of coherent air mass trajectories using a neural network—the case of dry intrusions. *Meteorological Applications*, 28(2), e1986. Available from: <https://doi.org/10.1002/met.1986>
- Smith, R.B. (1986) Further development of a theory of lee cyclogenesis. *Journal of Atmospheric Sciences*, 43(15), 1582–1602. Available from: [https://doi.org/10.1175/1520-0469\(1986\)043<1582:FDOATO>2.0.CO;2](https://doi.org/10.1175/1520-0469(1986)043<1582:FDOATO>2.0.CO;2)
- Somot, S., Houpert, L., Sevault, F., Testor, P., Bosse, A., Taupier-Letage, I. et al. (2018) Characterizing, modelling and understanding the climate variability of the deep water formation in the North-Western Mediterranean Sea. *Climate Dynamics*, 51, 1179–1210. Available from: <https://doi.org/10.1007/s00382-016-3295-0>
- Somot, S., Sevault, F., Déqué, M. & Crepon, M. (2008) 21st century climate change scenario for the Mediterranean using a coupled atmosphere–ocean regional climate model. *Global and Planetary Change*, 63(2–3), 112–126. Available from: <https://doi.org/10.1016/j.gloplacha.2007.10.003>
- Speranza, A., Buzzi, A., Trevisan, A. & Malguzzi, P. (1985) A theory of deep cyclogenesis in the lee of the Alps. Part I: modifications of baroclinic instability by localized topography. *Journal of Atmospheric Sciences*, 42(14), 1521–1535. Available from: [https://doi.org/10.1175/1520-0469\(1985\)042<1521:ATODCI>2.0.CO;2](https://doi.org/10.1175/1520-0469(1985)042<1521:ATODCI>2.0.CO;2)
- Sprenger, M. & Wernli, H. (2015) The LAGRANTO Lagrangian analysis tool—version 2.0. *Geoscientific Model Development*, 8(8), 2569–2586. Available from: <https://doi.org/10.5194/gmd-8-2569-2015>
- Tafferner, A. (1990) Lee cyclogenesis resulting from the combined outbreak of cold air and potential vorticity against the Alps. *Meteorology and Atmospheric Physics*, 43(1), 31–47. Available from: <https://doi.org/10.1007/BF01028107>
- Thorncroft, C.D., Hoskins, B.J. & McIntyre, M.E. (1993) Two paradigms of baroclinic-wave life-cycle behaviour. *Quarterly Journal of the Royal Meteorological Society*, 119(509), 17–55. Available from: <https://doi.org/10.1002/qj.49711950903>
- Tsidulko, M. & Alpert, P. (2001) Synergism of upper-level potential vorticity and mountains in Genoa lee cyclogenesis—a numerical study. *Meteorology and Atmospheric Physics*, 78(3–4), 261–285. Available from: <https://doi.org/10.1007/s703-001-8178-8>
- Waldman, R., Somot, S., Herrmann, M., Bosse, A., Caniaux, G., Estournel, C. et al. (2017) Modeling the intense 2012–2013 dense water formation event in the northwestern Mediterranean Sea: evaluation with an ensemble simulation approach. *Journal of Geophysical Research: Oceans*, 122(2), 1297–1324. Available from: <https://doi.org/10.1002/2016JC012437>
- Wernli, H. & Davies, H.C. (1997) A Lagrangian-based analysis of extratropical cyclones. I: the method and some applications. *Quarterly Journal of the Royal Meteorological Society*, 123(538), 467–489. Available from: <https://doi.org/10.1002/qj.49712353811>

**How to cite this article:** Givon, Y., Keller, D., Pennel, R., Drobinski, P. & Raveh-Rubin, S. (2024) Decomposing the role of dry intrusions for ocean evaporation during mistral. *Quarterly Journal of the Royal Meteorological Society*, 150(760), 1791–1808. Available from: <https://doi.org/10.1002/qj.4670>

## APPENDIX A. MISTRAL-DI ORIGINS

Large variability is held in the average DI trajectories, even within the different clusters. To further explore this variability within mistral–DI events, we examine the geographical origins of DIs entering the GOL. Geographical density plots of the DI trajectory at their starting times (0 hr in Figures 11 and 12) are presented. This view shows the location and orientation of the different DI trajectories included in the analysis. Different DI origins may alter the properties of mistral air masses and have implications for the momentum transport into the mistral, as discussed in the main text. The DI origins change drastically between the clusters and may fall to the west, north, or northeast of the GOL, at varying distances. Through most clusters, the DI origins appear divided between two primary hot spots: one over the North Atlantic, and another above the European continent. The latter can be centered at latitudes as high as 75° N (cluster 12) or as low as 50° N (cluster 11).

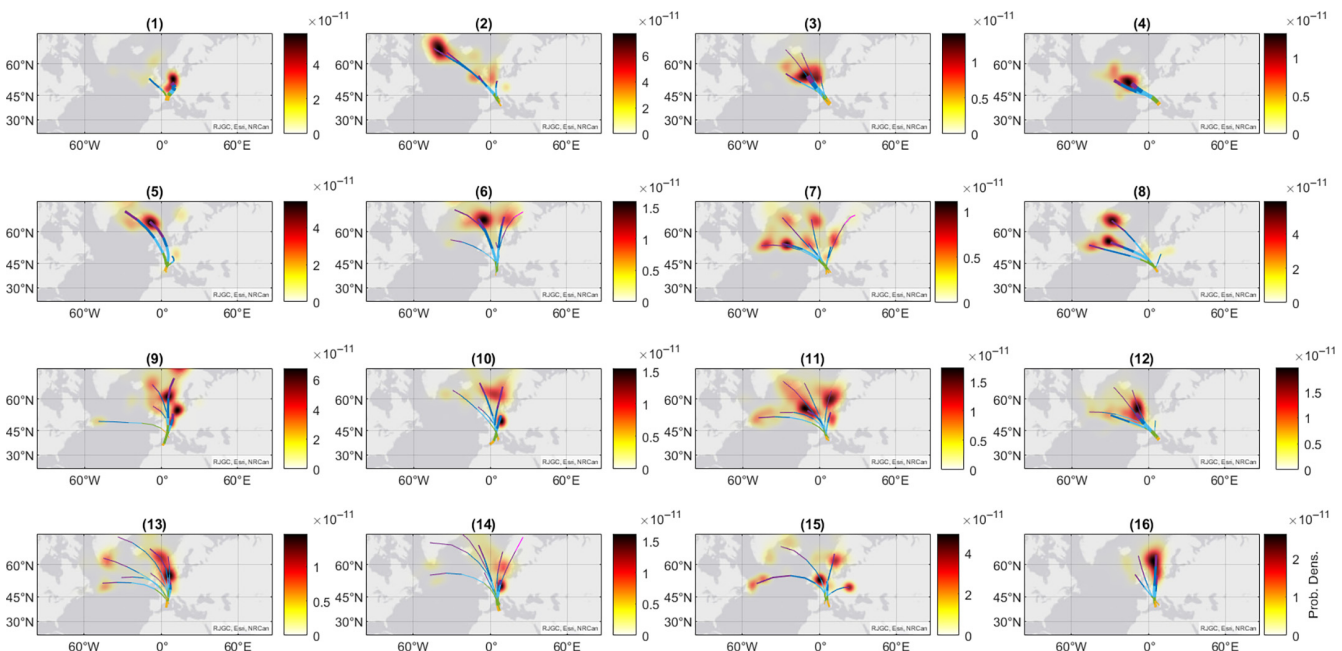


**FIGURE A1** Geographical probability density functions for the initial location of dry intrusion (DI) trajectories in every mistral cluster. The impact radius for the gridding is set to 500 km. DI trajectories, coloured by pressure (hPa), are averaged according to their starting positions on a grid of  $20^\circ \times 20^\circ$ , and the average trajectory density is shown for bins with more than 10 trajectories. The trajectory line width is proportional to the number of bin members.

## APPENDIX B. DRY-INTRUSION VERTICAL MOMENTUM FLUX AND ARRIVAL TIME

The schematic displayed in the main text (Figure 12) is supported by the Lagrangian analysis on the detected DI trajectories. Specifically, we separate DIs into two groups: those that enter the GOL target domain with VMF larger (i.e., more positive) than  $-1 \text{ [m}^2/\text{s}^{-2}\text{]}$  are denoted ‘DI 1’, while the rest compose ‘DI 2’. The results indeed show

that DI2 are steeper DIs that enter the DI target domain at earlier stages (10 h earlier, on average). This reinforces the view of VMF as the link between DIs and the mistral wind, sensitive to the DI slope. Figure B1 clarifies the important role of the time at which DIs enter the GOL on the resulting VMF in the GOL. As discussed in the main text, those DIs that arrive at the GOL at an earlier stage of their lifetime, deliver maximum vertical momentum fluxes and lead to extreme evaporation rates via increased wind speeds.

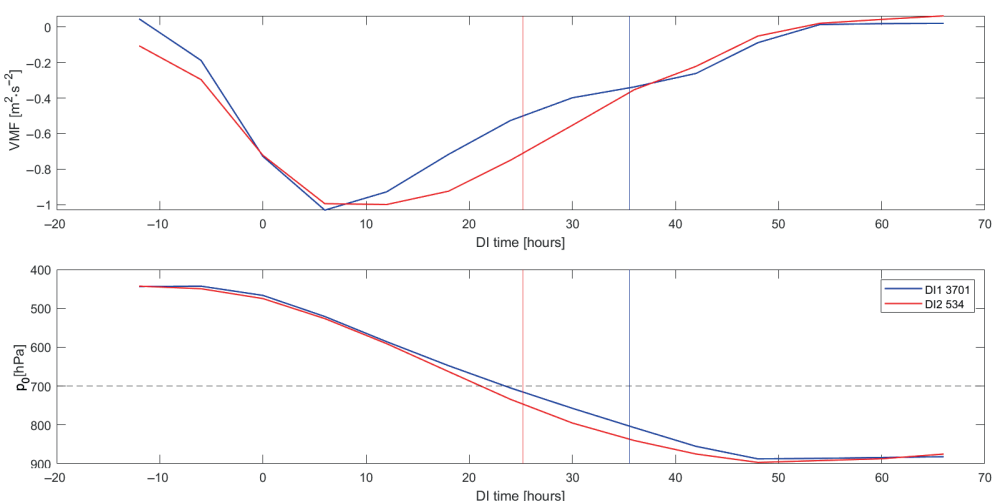


**FIGURE B1** Average vertical momentum flux (VMF) (top) and pressure (bottom) of the two DI groups, as a function of DI time (relative to initiation at  $t = 0$ ). Blue and red vertical lines denote the average arrival time of the DIs to the GOL. The number of DI trajectories in each group is given in the legend. The dashed line denotes the upper boundary of the target domain at the GOL.